

Optical Engineering

SPIDigitalLibrary.org/oe

Ultraviolet laser writing system based on polar scanning strategy to produce subwavelength metal gratings for surface plasmon resonance

Jun Amako
Eiichi Fujii

Ultraviolet laser writing system based on polar scanning strategy to produce subwavelength metal gratings for surface plasmon resonance

Jun Amako

Toyo University
2100 Kujirai, Kawagoe
Saitama 350-8585, Japan
E-mail: amako@toyo.jp

Eiichi Fujii

Seiko Epson Corporation
Fujimi 1010, Fujimi-cho
Nagano 399-0295, Japan

Abstract. We demonstrate the use of ultraviolet (UV) laser lithography in the production of subwavelength metal gratings. A laser writing system with a 413-nm Kr laser is used to write patterns on a resist-coated fused silica substrate mounted on a rotating table with a linear slider. One- and two-dimensional patterns are written in the resist at a selected sampling pitch or grating period, and the substrate is dry etched and coated with Au to obtain metallized gratings. Surface plasmon resonance dips, which appear in the reflectance spectra of the gratings, shift depending on the orientation of the incident polarization, because the gratings lack perfect symmetry owing to a system-induced skew in the writing beam. This dip shift can be considered tolerable when the gratings are used as a signal enhancer in Raman sensing applications. We conclude that UV laser writing based on polar coordinates is a candidate method for surface structuring on submicron scales. Devising a method to attain an unskewed beam will be the subject of future work. © The Authors. Published by SPIE under a Creative Commons Attribution 3.0 Unported License. Distribution or reproduction of this work in whole or in part requires full attribution of the original publication, including its DOI. [DOI: [10.1117/1.OE.52.6.063403](https://doi.org/10.1117/1.OE.52.6.063403)]

Subject terms: ultraviolet laser lithography; polar scanning strategy; subwavelength structures; metal gratings; surface plasmon resonance; biochemical sensing.

Paper 130373P received Mar. 8, 2013; revised manuscript received Apr. 17, 2013; accepted for publication May 14, 2013; published online Jun. 4, 2013.

1 Introduction

Subwavelength periodic structures (SWPS) with periods smaller than light wavelengths can control the intensity, phase, and polarization of light very effectively. They are highly useful for designing a variety of optical components, such as antireflection layers, wave plates, polarization separators, and local electric field enhancers.¹⁻⁴ Various lithography methods are available for producing SWPSs: electron beam writing, laser beam writing, laser interference exposure, and nanoimprinting. Each has advantages and disadvantages in terms of patterning accuracy, production throughput, and production cost. In laser writing, which is the subject of the present study, a beam can be scanned in the $x - y$ format⁵⁻⁷ or in the $r - \theta$ format.⁸⁻¹⁰ The most suitable format depends on the symmetries of the structures that need to be produced. The $x - y$ format is typically preferred when square symmetries are sought in the x and y directions; it can be applied to most one- and two-dimensional (2-D) patterns. The $r - \theta$ format is suitable for axial symmetry, and its high rotational speed makes it less time consuming, although it is not necessarily cost effective. A workpiece mounted on a table is rotated at a fixed speed throughout the laser exposure, except for short periods at the start and end.

We have developed an ultraviolet (UV) laser writing system based on a polar scanning strategy, and we have applied it to the fabrication of diffractive optical elements, which typically have micron-scale features. Elements with various beam delivery functions were evaluated for laser machining applications.¹¹⁻¹⁴ Furthermore, we have explored our

system's potential for use in submicron-scale patterning, and we have examined the effects of pattern errors caused by the polar format. Provided that such errors do not compromise the performance of the SWPSs, this versatile writing system can be extended to the production of subwavelength-scale optical elements.

We report a lithography process by which the polar-format laser writing system forms metal gratings at submicron scales. These gratings can cause surface plasmon resonance (SPR), which appears as a dip in the zeroth-order reflection at the air/grating interface. By observing SPR dips carefully, we can figure out what would happen if there were system-induced fabrication errors. In the next section, the error factors that are pertinent to the polar strategy are described, and sample metal gratings produced with the laser writing system are discussed. In Sec. 3, reflectance spectra obtained from the gratings are presented, and in Sec. 4, the effects of fabrication errors on the far-field responses are discussed. Simple but effective formulas that we have derived explain how SPR characteristics depend on incident polarization and can be applied in general discussions over plasmonic gratings.

2 Production of Metal Gratings

As schematically depicted in Fig. 1, the laser writing system comprises a rotating table and a slider, and it can write patterns on resist in a polar format by synchronizing the movements of the table and the slider.¹⁵ The system has a Kr⁺ laser source with a wavelength of 413 nm. The exciting beam is focused at $0.5 \mu\text{m}$ in width ($1/e^2$) by a high-numeric-aperture objective lens, and the resist is exposed

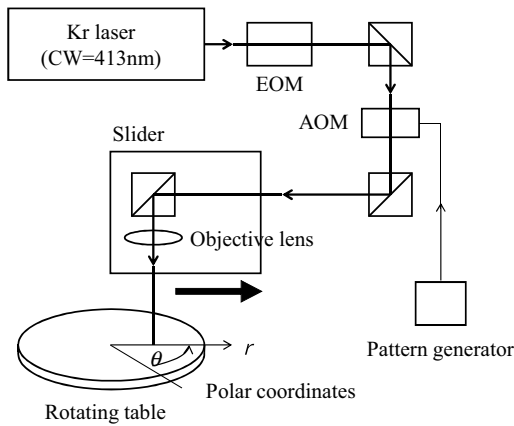


Fig. 1 Schematic of laser writing system with polar coordinates.

to the focused beam. The beam intensity is roughly adjusted by an electro-optic modulator and finely tuned at 266 levels by an acousto-optic modulator (AOM), which is turned on and off at a fixed rate of 2.9 MHz. This rate determines the sampling frequency in the resist patterning in the angular direction. The duty cycle for switching the AOM is set at 25%, 50%, or 75%, taking into account the selected sampling pitch or grating period, and no mechanism for independent beam width adjustment is available in the radial direction. Consequently, the effective writing beam footprint can be skewed in either the radial direction or the scan direction. When a laser linear scale is used, the substrate can be positioned with a 3-nm resolution in the radial direction. The patterning time is determined by the patterns being drawn. We have tested this system by writing linear, tetragonal, and hexagonal patterns with submicron periods.

With the polar coordinates employed in the system, as illustrated in Fig. 2, the grating period $P(r)$ in the angular direction is given by

$$P(r) = r\omega/f, \quad (1)$$

where r is the radius, ω is the angular velocity, and f is the sampling frequency. The grating period is 500 nm at a radius of 62 mm, for example, with an angular velocity of 24 rad/s or a rotational speed of the table of 225 rpm. The sampling frequency in the angular direction is 2.9 MHz. By differentiating Eq. (1), we can derive $\Delta P = (\omega/f)\Delta r$, where Δr is the deviation in the radius, and ΔP is the deviation in the grating period. This relation between ΔP and Δr is shown

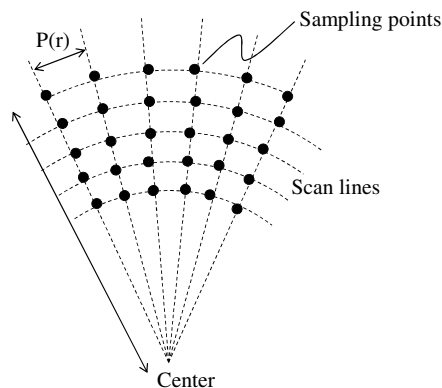


Fig. 2 Polar coordinates and sampling points.

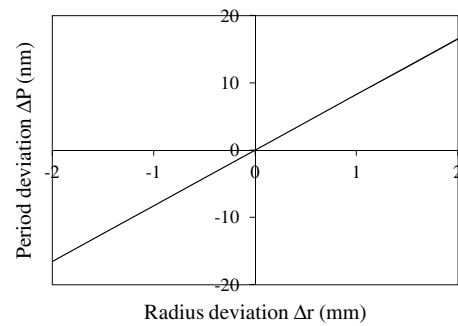


Fig. 3 Grating period deviation versus radius deviation.

in Fig. 3. We estimate ΔP at ~ 8 nm for $\Delta r = 1$ mm, and ΔP is negligible when Δr is 10 μm or less, which is a typical size of the sensing region on a metal grating used in Raman sensing.^{16,17} Note that, for a fixed Δr , ΔP remains constant, regardless of r . This polar scanning strategy makes use of $\sim 70\%$ of the entire area of a glass substrate 200 mm in diameter. Gratings are formed with a radius of 49 to 98 mm on the substrate, and the grating period varies from 400 to 800 nm in the angular direction. These periods are suitable for metal gratings used at visible wavelengths.

By using the laser writing system described above, metal gratings were fabricated as follows. A positive-type photoresist layer was spin-coated to a thickness of 100 nm on a fused silica substrate with a thickness of 1.2 mm and a diameter of 200 mm. The resist-coated substrate mounted on the rotating table was exposed to a focused UV laser beam. The grating patterns were written in a 3-mm wide circular region using a ~ 0.5 - μm wide focused beam at a sampling frequency of 2.9 MHz. With the rotational speed fixed at 225 rpm, the radii for periods of 400, 500, and 600 nm were set at 49, 62, and 74 mm, respectively. The exposed resist was developed in a developer, rinsed in running deionized water, and dried in air to form the resist patterns on the substrate. Then, using the patterned resist as a mask, the fused silica surface was etched by reactive ion etching. When C_2F_6 , CF_4 , and CHF_3 were used as process gases, the obtained etch rates were 150 nm/min for resist and 240 nm/min for fused silica, and the etching selectivity was 1.6. Because this was an adequate selectivity, no metal mask was placed between the resist and the substrate. The resist was removed by dry etching with O_2 to obtain fused silica gratings. A 3-nm thick adhesive layer of Cr was formed on the fused silica corrugations by vacuum deposition; then, a 100-nm thick plasmonic layer of Au was formed by sputtering. The Au layer was sufficiently thick to prevent incoming light from passing through the gratings. We selected Au for coverage because it remains stable in air, and its dielectric constants enable efficient excitation of surface plasmons at visible wavelengths. Other candidate metals are Ag, Ni, and Al.

Figure 4 shows atomic force microscopy images of sub-wavelength metallized gratings produced with the polar scanning system. They are tetragonal arrays of (a) holes and (b) pillars, and hexagonal arrays of holes (c) 320-nm wide and (d) 230-nm wide. All these gratings had a common period of 500 nm, and the corrugations were 50 nm or less in depth. The fill factors in Fig. 4(c) and 4(d) were 0.64 and 0.46, respectively. When tetragonal patterns were drawn, the sampling points on the scan lines were aligned in phase,

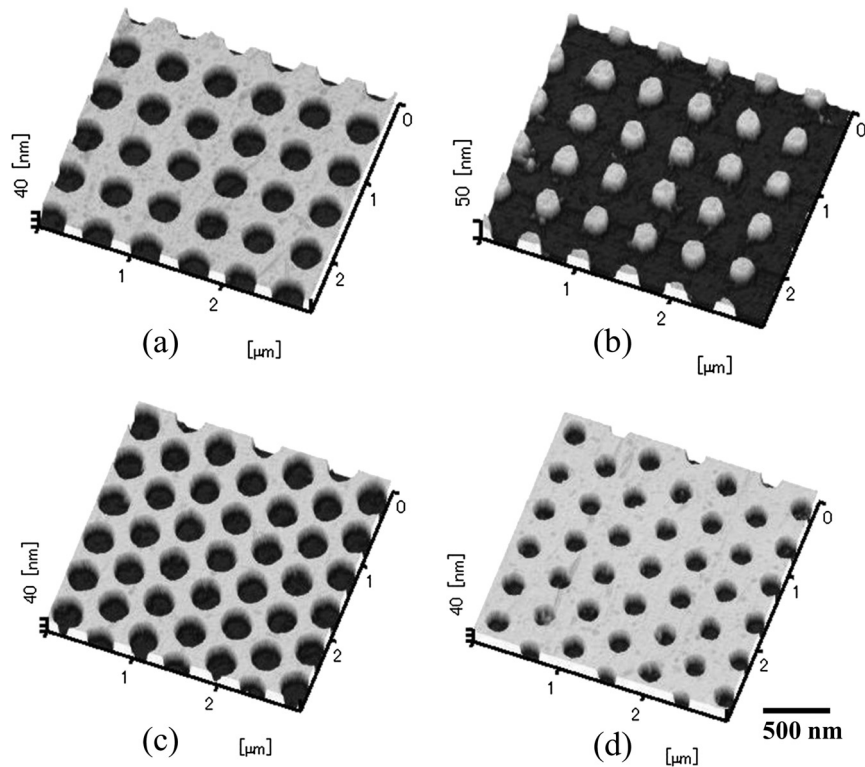


Fig. 4 Atomic force microscopy images of metallized gratings: tetragonal arrays of (a) holes and (b) pillars and hexagonal arrays of holes (c) 320-nm wide and (d) 230-nm wide. The scale bar is common to all panels.

radially, around the rotating center. For hexagonal patterns, the sampling points were aligned out of phase by half a sampling pitch between adjacent scan lines. As a result, the tetragonal gratings had a constant period in the radial direction and a varying period in the angular direction as a function of the radius. The hexagonal gratings had different periods among the three principal directions crossing at 60 deg. Tuning of the exposure beam intensity allowed for the formation of holes and pillars and for the adjustment of fill factors in the range of 0.3 to 0.7. The one-dimensional gratings we fabricated had a fixed period across their grooves, though they are not shown.

3 Experiment and Results

Reflectance spectra or zeroth-order reflections were obtained by illuminating a metal grating with a collimated white light. The light spot was 2-mm wide and was centered at the radius for a grating period of interest. Within the spot, the grating period varied in the angular direction by at most ± 8 nm. Those spectra were captured using a spectrometer (USB2000, Ocean Optics) against incident polarization orientation θ . The 0-deg orientation was set perpendicular to the polar scanning lines. A 10- μm wide slit was used on the spectrometer. A spectrum from a nonstructured area of the Au layer was used as a reference signal to normalize the spectra from the gratings. We performed computational analyses using the finite-difference time-domain (FDTD) method to compare the theoretically predicted reflectance spectra with the experimental results.

Figure 5 shows the reflectance spectra obtained from a tetragonal grating (hole array) with a 600-nm period at its center for $\theta = 0, 45,$ and 90 deg. A grating depth of

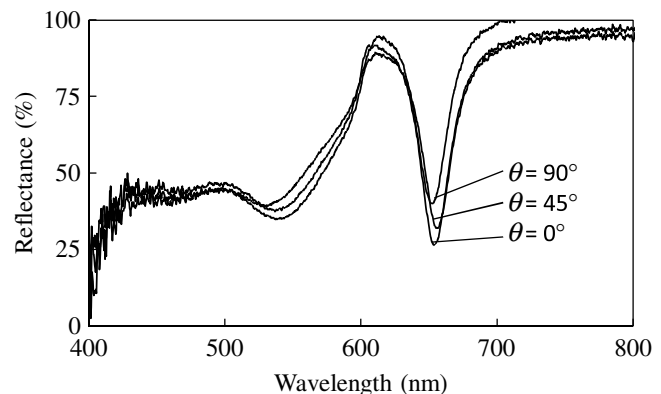


Fig. 5 Reflectance spectra from a 600-nm period tetragonal grating.

80 nm was chosen. At that depth, the SPR dip bottomed out, according to the FDTD analysis. SPR dips mediated by the (1, 0) and (0, 1) modes of evanescent waves appeared at around 650 nm. The reflectance minimum (dip depth) varied from 25% to 40%, and the wavelength for the minimum (dip wavelength) shifted by ~ 5 nm over the range of 0 to 180 deg for incident electric vector orientation. The wavelength shift was much smaller than the ~ 30 -nm FWHM of the dip. In theory, neither the dip depth nor the dip wavelength should change, regardless of the incident polarization orientation, provided the arrays have perfect tetragonal symmetry.

Figure 6 shows the reflectance spectra obtained from a hexagonal grating (hole array) with a 600-nm period at its center for $\theta = 0, 60,$ and 120 deg. A grating depth of 120 nm was selected according to the results of the FDTD

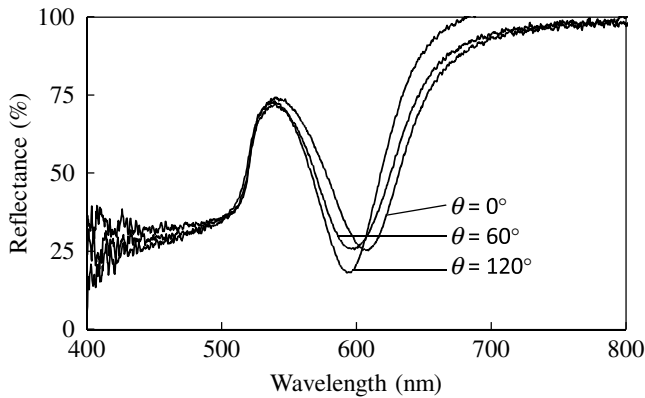


Fig. 6 Reflectance spectra from a 600-nm period hexagonal grating.

analysis. SPR dips, which were caused by the $(1/2, 3/2)$, $(1, 0)$, and $(1/2, -3/2)$ modes of evanescent waves, emerged at 590 to 610 nm. The reflectance at the dip varied from 17% to 27% over the range of 0 to 180 deg for incident electric vector orientation. The dip wavelength shifted by ~ 15 nm, which was smaller than the dip width of ~ 60 nm. When the hexagonal structures are identical in the three principal directions, $\theta = 30, 90,$ and 150 deg, the dip depth and dip wavelength should remain unchanged, regardless of the polarization orientation.

Figure 7 shows the SPR dip behavior as a function of the incident polarization orientation, in terms of (a) dip depth and (b) dip wavelength, for the 600-nm period tetragonal grating. These data are taken from Fig. 5. In Fig. 7(a), the reflectance changed in a cycle of ~ 90 deg, and the difference between the maximum (weak resonance) and minimum (strong resonance) was $\sim 15\%$. We evaluated several samples

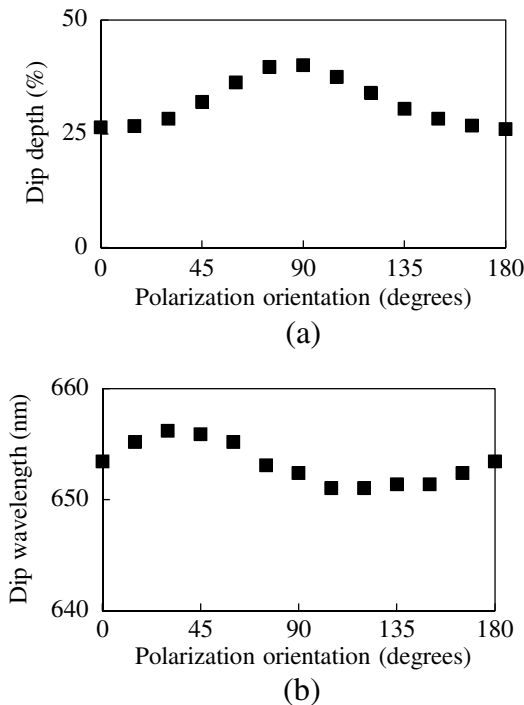


Fig. 7 SPR dip behavior as a function of incident polarization orientation for the tetragonal grating whose spectra are shown in Fig. 5: (a) dip depth and (b) dip wavelength.

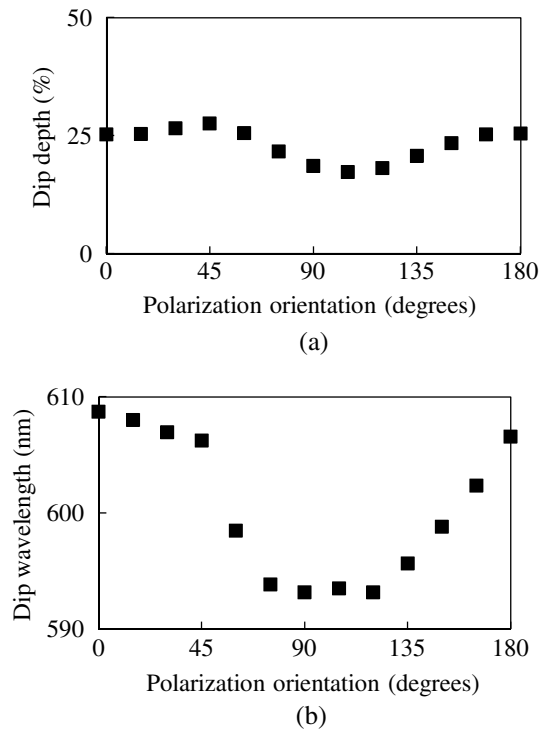


Fig. 8 SPR dip behavior as a function of incident polarization orientation for the hexagonal grating whose spectra are shown in Fig. 6: (a) dip depth and (b) dip wavelength.

and found that the reflectance always had a maximum at around $\theta = 90$ deg. The results shown in Fig. 7(a) indicate that the holes could have been somewhat skewed in one of two directions. In Fig. 7(b), the dip wavelength was 651 to 656 nm; thus, the dip shift was ~ 5 nm for the range of 0 to 180 deg for the polarization orientation. We have not yet established any relation between the two curves shown in Fig. 7(a) and 7(b).

Figure 8 shows the SPR dip behavior as a function of incident polarization orientation, in terms of (a) dip depth and (b) dip wavelength, for the 600-nm period hexagonal grating. These data are taken from Fig. 6. In Fig. 8(a), the reflectance changed from 17% to 27% in a cycle of ~ 90 deg. The reflectance did not necessarily have a maximum at 90 deg, in contrast with the tetragonal gratings. The results shown in Fig. 8(a) indicate that the hole arrays could have been somewhat deformed in three directions: 30, 90, and 150 deg. In Fig. 8(b), the dip wavelengths were 594 to 609 nm, and the wavelength shift was ~ 15 nm for the range of 0 to 180 deg for the polarization orientation. We have found no proof of any significant relation between the two curves shown in Fig. 8(a) and 8(b).

4 Discussion

Because surface plasmons are excited by evanescent waves generated in a metallized grating, the dip depth (reflectance minimum) is undoubtedly associated with the coupling efficiency of incident light into evanescent waves. The reflectance R and coupling efficiency C can be approximately related as $R = 1 - C$ if bulk absorption in the metal is neglected. Given this assumption, the reflectance for tetragonal gratings, $R_t(\theta)$, can be defined by

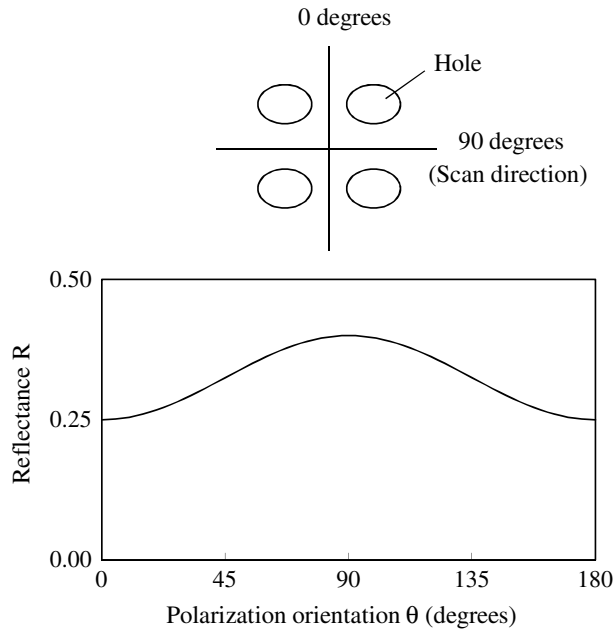


Fig. 9 Reflectance as a function of incident polarization orientation for a tetragonal grating (computer simulation).

$$R_t(\theta) = (1 - C_1)\cos^2(\theta) + (1 - C_2)\sin^2(\theta), \quad (2)$$

where θ is the incident polarization orientation, and C_1 and C_2 are the coupling efficiencies at $\theta = 0$ deg and $\theta = 90$ deg, respectively. $R_t(\theta)$ is plotted as a function of θ in Fig. 9 for $C_1 = 0.75$ and $C_2 = 0.60$. The reflectance varies in a cycle of 90 deg and has a maximum of ~ 0.4 at 90 deg, which agrees with the measurement results shown in Fig. 7(a). For $C_1 = C_2$, the reflectance obviously remains constant and independent of θ . By comparing the experimental results shown in Fig. 7(a) with the simulation results shown in Fig. 9, we find that the incident light was actually coupled with the evanescent waves at different efficiencies in the 0- and 90-deg directions.

Likewise, the reflectance for hexagonal gratings, $R_h(\theta)$, can be defined as

$$R_h(\theta) = (1 - C_1)\cos^2(30 - \theta) + (1 - C_2)\cos^2(90 - \theta) + (1 - C_3)\cos^2(150 - \theta), \quad (3)$$

where C_1 , C_2 , and C_3 are the coupling efficiencies for the evanescent waves at $\theta = 30$ deg, $\theta = 90$ deg, and $\theta = 150$ deg, respectively. $R_h(\theta)$ is plotted as a function of θ in Fig. 10 for $C_1 = 0.75$, $C_2 = 0.90$, and $C_3 = 0.90$. The calculated reflectance changes in a cycle of 90 deg and has a maximum of ~ 0.30 at 30 deg, in agreement with the measured reflectance. The assumption that $C_1 \neq C_3$ is warranted because the array pitch depends on the radius. For $C_1 = C_3$, the reflectance peaks at 90 deg, and for $C_1 = C_2 = C_3$, the reflectance remains constant regardless of θ . The measurements shown in Fig. 8(a) and the simulations shown in Fig. 10 together lead us to believe that the evanescent waves were in fact generated at different efficiencies in three directions: $\theta = 30$ deg, $\theta = 90$ deg, and $\theta = 150$ deg.

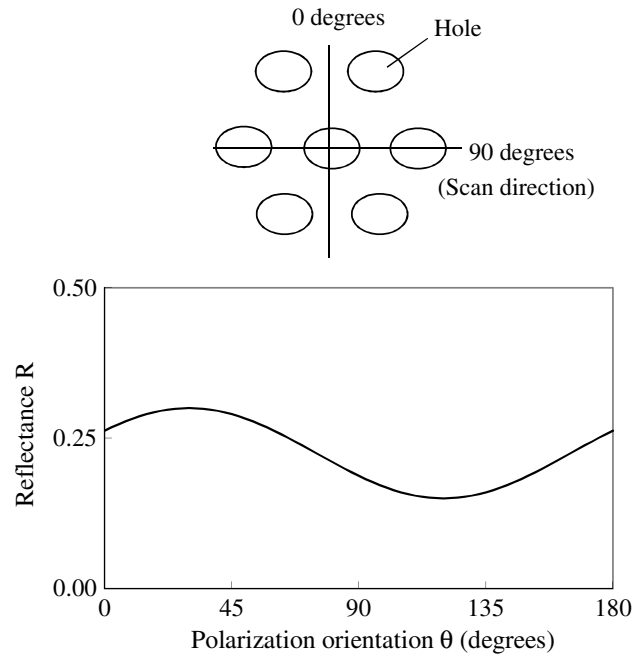


Fig. 10 Reflectance as a function of incident polarization orientation for a hexagonal grating (computer simulation).

The coupling efficiencies are related to two factors: the period and surface-relief profile of a grating. They determine an optimal depth at which the efficiency peaks. The period deviation within the spectrum acquisition area was ~ 8 nm (see Sec. 2), which was extremely small to affect the efficiencies. Any possible differences in grating profile between the two directions, which could have been caused by the skewed writing beam, were very likely to cause the efficiency gap. The reflectance formulas described above, though rather simple, explain the observed behaviors of the SPR dips.

Using the plasmonic dispersion relation for a smooth air/metal interface,¹⁸ the resonance wavelength λ is given by

$$\lambda = P\{\varepsilon(\lambda)/[1 + \varepsilon(\lambda)]\}^{1/2}, \quad (4)$$

where P is the grating period and $\varepsilon(\lambda)$ is the dielectric constant of the metal. This equation indicates that the peak wavelength is proportional to the grating period. In the angular direction, the period varies from $P - \Delta P$ to $P + \Delta P$ because of the grating layout used, and the integrated period deviation across the illuminated area on a grating becomes zero by making a small- ΔP approximation of Eq. (4). On the basis of this premise, it would be fair to say that the period deviation was not the chief cause of the observed wavelength shift. What is probably the case is that the grating profiles are made less symmetrical when drawn by a skewed beam; hence, the dispersion curves of the gratings are modified, leading to the observed dip wavelength shifts. A straightforward but delicate method of avoiding a skewed beam is to use a slit.¹⁹ There is little or no hardware flexibility in terms of making the duty cycle of the AOM control signal variable. A discussion of the SPR characteristics of deformed hole arrays is beyond the scope of the current study.

Is the behavior of the SPR dips observed in our experiment suitable for practical applications? The answer has much to do with how the metallized gratings are applied.

The gratings can be applied as a near-field enhancer to amplify Raman signals. Propagating surface plasmons excited with the gratings are accompanied by enhanced electric fields near their corrugated surfaces, at which Raman signals from target analytes are amplified.^{20–22} When 2-D gratings are used in Raman sensing, which is our interest, the use of circular polarization is reasonable, because the optical responses of a spectrometer are usually subject to the polarization of the input signals. In that case, the SPR dips at all orientations would be averaged out, suggesting that using the dip depth or the dip wavelength as a measure of the target molecules would be problematic.

5 Conclusion

We investigated the potential of using a polar scanning strategy for laser-beam writing of SWPSs. We produced metalized gratings using our laser writing system with polar coordinates, and we measured their SPR characteristics. In our measurements, SPR dips were observed near the theoretically predicted wavelengths, and yet, for 2-D gratings, the dip depth changed by ~ 2 times its minimum, whereas the dip wavelength shifted by ~ 20 nm for different orientations of incident linear polarization. The dip shifts occurred because of the skewed writing beam footprint; they were extremely large to be attributed to the polar format. The observed dip shifts can be tolerated when the gratings are used as signal enhancers in Raman sensing applications. We conclude that UV laser lithography based on this polar scanning strategy is a candidate method for surface structuring on submicron scales. Future research work should be aimed at devising a method for realizing an unskewed beam footprint without any dependence on the grating period.

References

1. H. Toyota et al., "Fabrication of microcone array for antireflection structured surface using metal dotted pattern," *Jpn. J. Appl. Phys.* **40**(7), L747–L749 (2001).
2. X. Deng et al., "Achromatic wave plates for optical pickup units fabricated by use of imprint lithography," *Opt. Lett.* **30**(19), 2614–2616 (2005).
3. V. Pelletier et al., "Aluminum nanowire polarizing grids: fabrication and analysis," *Appl. Phys. Lett.* **88**(21), 211114–211116 (2006).
4. S. M. Kim, W. Zhang, and B. T. Cunningham, "Coupling discrete metal nanoparticles to photonic crystal surface resonant modes and application to Raman spectroscopy," *Opt. Express* **18**(5), 4300–4309 (2010).
5. M. Haruna et al., "Laser beam lithographed micro-Fresnel lenses," *Appl. Opt.* **29**(34), 5120–5126 (1990).
6. M. T. Gale et al., "Fabrication of continuous-relief micro-optical elements by direct laser writing in photoresist," *Opt. Eng.* **33**(11), 3556–3566 (1994).
7. Y. C. Chen et al., "Development and applications of a laser writing lithography system for maskless patterning," *Opt. Eng.* **37**(9), 2521–2530 (1998).
8. T. Yatagai, J. G. Camacho-Basilio, and H. Onda, "Recording of computer generated holograms on an optical disk master," *Appl. Opt.* **28**(6), 1042–1044 (1989).
9. A. G. Poleshchuk et al., "Polar coordinate laser pattern generator for fabrication of diffractive optical elements with arbitrary structure," *Appl. Opt.* **38**(8), 1295–1301 (1999).
10. S. Reicheit et al., "Wavefront aberrations of rotationally symmetric CGHs fabricated by a polar coordinate laser plotter," *J. Mod. Opt.* **49**(7), 1069–1087 (2002).
11. J. Amako, T. Shimoda, and K. Umetsu, "Versatile light-control schemes based on diffractive optics for laser drilling, cutting, and joining technologies for microelectronic and micromechanical components and devices," *Proc. SPIE* **5339**, 475–487 (2004).
12. J. Amako et al., "Laser-based micro-processes using diffraction-free beams generated by diffractive axicons," *Proc. SPIE* **5713**, 497–507 (2005).
13. J. Amako et al., "Use of non-digitized diffractive optical elements for high-throughput and damage-free laser materials processing," *Proc. SPIE* **6107**, 6107D1 (2006).
14. K. Nagasaka, E. Fujii, and J. Amako, "Laser-based micro-bonding of VCSELs using arrayed beams from a fiber laser," *Proc. SPIE* **6880**, 6880O1 (2008).
15. J. Amako, K. Nagasaka, and E. Fujii, "Direct laser-writing of diffractive array illuminators operable at two wavelengths," *Proc. SPIE* **4416**, 360–363 (2001).
16. K. T. Carron et al., "Resonances of two-dimensional particle gratings in surface-enhanced Raman scattering," *J. Opt. Soc. Am. B* **3**(3), 430–440 (1986).
17. K. Kneipp et al., "Single molecule detection using surface-enhanced Raman scattering (SERS)," *Phys. Rev. Lett.* **78**(9), 1667–1670 (1997).
18. H. Rother, *Surface Plasmons on Smooth and Rough Surfaces and on Gratings*, Springer-Verlag, Berlin (1988).
19. M. Ams et al., "Slit beam shaping method for femtosecond laser direct-write fabrication of symmetric waveguides in bulk glasses," *Opt. Express* **13**(15), 5676–5681 (2005).
20. M. Arnold et al., "Enhanced Raman scattering from benzene condensed on a silver grating," *J. Mod. Opt.* **39**(11), 2329–2346 (1992).
21. I. Baltog, N. Primeau, and R. Reinisch, "Surface-enhanced Raman scattering on silver grating: optimized antennalike gain of the stokes signal of 10^4 ," *Appl. Phys. Lett.* **66**(10), 1187–1189 (1995).
22. M. Kahl et al., "Periodically structured metallic substrates for SERS," *Sens. Actuators B* **51**(3), 285–291 (1998).

Biographies and photographs of the authors are not available.